# Proposal on Millimeter-Wave Channel Modeling for 5G Cellular System

Sooyoung Hur, *Member, IEEE*, Sangkyu Baek, *Member, IEEE*, Byungchul Kim, *Member, IEEE*, Youngbin Chang, *Member, IEEE*, Andreas F. Molisch, *Fellow, IEEE*, Theodore S. Rappaport, *Fellow, IEEE*, Katsuyuki Haneda, *Member, IEEE*, and Jeongho Park, *Member, IEEE*

***Abstract*—This paper presents 28 GHz wideband propagation channel characteristics for millimeter wave (mmWave) urban cellular communication systems. The mmWave spectrum is considered as a key-enabling feature of 5G cellular communication systems to provide an enormous capacity increment; however, mmWave channel models are lacking today. The paper compares measurements conducted with a spherical scanning 28 GHz channel sounder system in the urban street-canyon environments of Daejeon, Korea and NYU campus, Manhattan, with ray-tracing simulations made for the same areas. Since such scanning measurements are very costly and time-intensive, only a relatively small number of channel samples can be obtained. The measurements are thus used to quantify the accuracy of a ray-tracer; the ray-tracer is subsequently used to obtain a large number of channel samples to fill gaps in the measurements. A set of mmWave radio propagation parameters is presented based on both the measurement results and ray-tracing, and the corresponding channel models following the 3GPP spatial channel model (SCM) methodology are also described.**

***Index Terms*—mmWave, 28GHz, channel measurement, spherical scans, propagation, SCM, channel model, path loss models, PDP.**

## I. Introduction

THE mmWave band will be a key component in the next generation wireless communication systems (5G). It enables the use of more spectrum [3]–[6] to support greater data traffic for various multimedia services, such as broadband mobile and backhaul services. Fundamental knowledge of the channel propagation characteristics in this new frequency band is vital for developing 5G wireless communications technology.

Many mmWave channel measurement campaigns have recently been performed to assess the feasibility of mmWave outdoor cellular access communications, yielding empirically-based path loss and delay dispersion properties since the 1990s [8]–[12] in both outdoor and indoor environments. In the 2000s, interest included the directional characteristics more, in order to assess the ability of adaptive beamforming to increase the SNR [3], [13]–[15]. Research projects including industry and academia, such as METIS [16], MiWEBA [17], NYU WIRELESS [18]–[22] and mmMagic [23] have been developing 5G channel propagation models including mmWaves. In these projects, many scenarios are considered using mmWave frequencies, such as street-canyon and open square in urban outdoor cellular environments and shopping malls, open/closed indoor office environments, and stadium scenario.

Recently, measurement campaigns in urban environments, e.g., in Daejeon, Korea [24] and Manhattan, New York, USA [5], [18], [25], [26], were conducted with directional channel sounders, under participation of some of the authors. The relatively small measured propagation data sets must be extended using simulation-based analysis to extract spatial and temporal channel model parameters in urban cellular environments. As an alternative approach, we consider in this paper a ray-tracing-based method to extend the sparse empirical datasets and to analyze the mmWave channel characteristics. Propagation prediction using ray-tracing simulations is a popular approach for modeling physical channels because it is available to investigate most of the propagation mechanisms of wireless channels, such as reflection and diffraction, and inherently provides directionally resolved spatial characteristics [27]. Although ray-tracing simulations often suffer some geometry data base errors and do not always include all of the relevant propagation mechanisms, such as non-specular scattering effects, ray-tracing results have been successfully used to model wireless radio propagation [7], [27]–[30], and will become more important at mmWave frequencies, where scattering becomes more dominant than diffraction [31]. In this work, we verify that the ray-tracing simulations provide good agreement with measurement results over all of the measured distances, as we compared simulations with measurements in the same environment and distance ranges for verification.

In [32], an overview of channel modeling approaches in mmWave is provided, and the geometry-based stochastic channel model used in 3GPP is considered in this paper, which offers an evaluation methodology for the mmWave band with reasonable compromise between accuracy and complexity. This paper focuses on characterizing mmWave propagation models

Manuscript received June 01, 2015; revised November 27, 2015; accepted January 07, 2016. Date of publication February 08, 2016; date of current version April 14, 2016. This paper was presented in part at the EuCAP 2015, Lisbon, Portugal, April 13–17, 2015 [1] and ICC Workshop, London, June 2015 [2]. The guest editor coordinating the review of this manuscript and approving it for publication was Prof. Sundeep Rangan.

S. Hur, S. Baek, B. Kim, C. Chang, and J. Park are with Samsung Electronics, Suwon 443-742, Korea (e-mail: sooyoung.hur@samsung.com; sangkyu.baek@samsung.com; bc1117.kim@samsung.com; yb.chang@samsung.com; jeongho.jh.park@samsung.com).

A. F. Molisch is with the Department of Electrical Engineering, University of Southern California, Los Angeles, CA 90034 USA (e-mail: molisch@usc.edu).

T. S. Rappaport is with NYU WIRELESS and New York University, New York, NY, USA (e-mail: tr51@nyu.edu).

K. Haneda is with Aalto University, Aalto 02015, Finland (e-mail: katsuyuki.haneda@aalto.fi).

Color versions of one or more of the figures in this paper are available online at http://ieeexplore.ieee.org.

Digital Object Identifier 10.1109/JSTSP.2016.2527364

1932-4553 © 2016 IEEE. Personal use is permitted, but republication/redistribution requires IEEE permission.
See http://www.ieee.org/publications_standards/publications/rights/index.html for more information.
Authorized licensed use limited to: K & L Gates. Downloaded on October 21,2025 at 14:40:17 UTC from IEEE Xplore. Restrictions apply.
MASSIVELY BROADBAND, IPR2026-00035, Ex.2014, Page 1 of 16

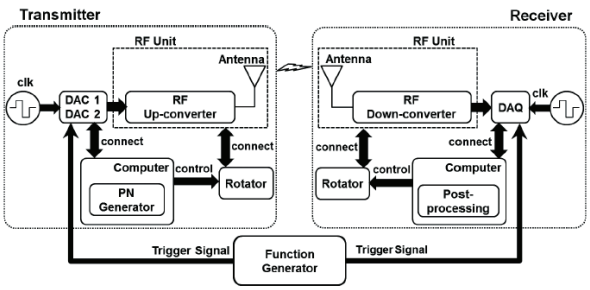


(a) Measurement System Block Diagram

(b) Channel Sounder with Positioning Rotator

Fig. 1. 28 GHz Synchronized Channel Sounder.

including both angular (azimuth and elevation) and delay domain channel parameters to develop a double-directional wideband channel model in the 28 GHz band. First, we summarize measurement approaches and results, as well as the ray-tracing results, aimed towards achieving a complete 28 GHz spatial channel model (SCM) targeted for the street-canyon scenario in urban outdoor cellular environments. To extract the channel model parameters, we adapt the methodology of the statistical SCM used in 3GPP [33]–[35]. While other promising statistical approaches for 3GPP-style channel models have been developed from measured data [18], [20], we do not address those approaches here. As our main result, we show an exemplary parameterization of a double-directional channel model in the 28 GHz mmWave band in urban cellular street-canyon scenarios.

## II. Measurements and Ray-tracing in Urban Scenario

### A. Channel Sounding Measurements

The wideband radio channel at 28 GHz was measured using two similar correlation-based channel sounders (one at NYU and one at Samsung), capable of recovering the channel impulse response (CIR) over 200 m TX-RX distances in NLoS environment. A schematic of the Samsung's sounder is shown in Fig. 1, see also [18], [36] for more details of the channel sounders. The sounder in Fig. 1 transmitted a 250 Mega chipper-second (Mcps) pseudonoise (PN) sequence, resulting in a multipath delay resolution of 4 ns. Horn antennas with 24.5 dBi gain and 10-degree half-power beamwidth were connected to the TX and RX radio frequency (RF) front ends. Both the TX and RX sides were equipped with an antenna steering rotator that controlled the beam pointing direction over the azimuth and elevation dimensions automatically with a synchronized triggering signal. Additional Samsung channel sounder specifications are given in Table I (the NYU sounder was similar and used a 400 Mcps clock rate to provide 2.5 ns resolution, see [5], [18]).

TABLE I
28 GHz Channel Sounder Specification

| Parameter | Value |
|---|---|
| Carrier Frequency | 27.925 GHz |
| Signal Bandwidth | 250 MHz |
| Transmit Power | 29 dBm |
| Horn Antenna Beamwidth | 10 degrees |
| Horn Antenna Gain | 24.5 dBi |
| Antenna Polarization | Linear Polarization |

The channel sounder uses rotatable horn antennas with high gain and high directivity in order to detect the signals in mmWave band over a few hundred meters. However, due to the limited beamwidth of these antennas, multiple angular measurements are required to cover all directions, and a synthesizing process is used to generate omni-directional characteristics [20], [36]. For a particular measurement location in Daejeon, 50 directional power delay profiles (PDPs) are recorded at each TX and RX steering angle bin; the angle bin width is set equal to the half-power beamwidth of the antenna, and angle bins are scanned over azimuthal/elevation angles in increments of the width of angular bin. The measured angular PDP at the $i$-th and $j$-th angle bin is then obtained from CIR by detecting peaks corresponding to propagation paths, similar to the 28 GHz measurement procedure used at NYU [5]. Each directional PDP has an aligned time-stamp, which allowed us to superimpose directional PDPs on an absolute time axis with the appropriate relative time difference of each directional measurement in order to synthesize omni-directional PDPs. To avoid overestimating path power, omni-directional PDPs are synthesized by detecting max-power paths on superimposed PDPs. The algorithm of synthesized omni PDP is verified by comparison between the synthesized omni PDP and the PDP of omni-directional measurement in short distance. The timing error in synthesized PDP was observed to be within 1 ns [36]. It is noted that the omni-directional received power and path loss are accurately estimated by summing the power of all synthesized paths [21].

### B. Measurement Campaign and Simulation in Urban Street Canyon Environment

A measurement campaign was performed in an urban street canyon in Daejeon, Korea [24]. Figure 2 shows a bird's eye view of the urban area showing the TX and RX locations and the measured path loss result. The synchronous channel sounder system described in the previous section was used for channel measurements over 200 m distance range in the urban area. The TX was placed on the fifth floor (15 m above ground) of a building rotating in the azimuth and elevation dimensions, and the RX placed on the top of a vehicle at street-level (1.6 m

Authorized licensed use limited to: K & L Gates. Downloaded on October 21,2025 at 14:40:17 UTC from IEEE Xplore. Restrictions apply.

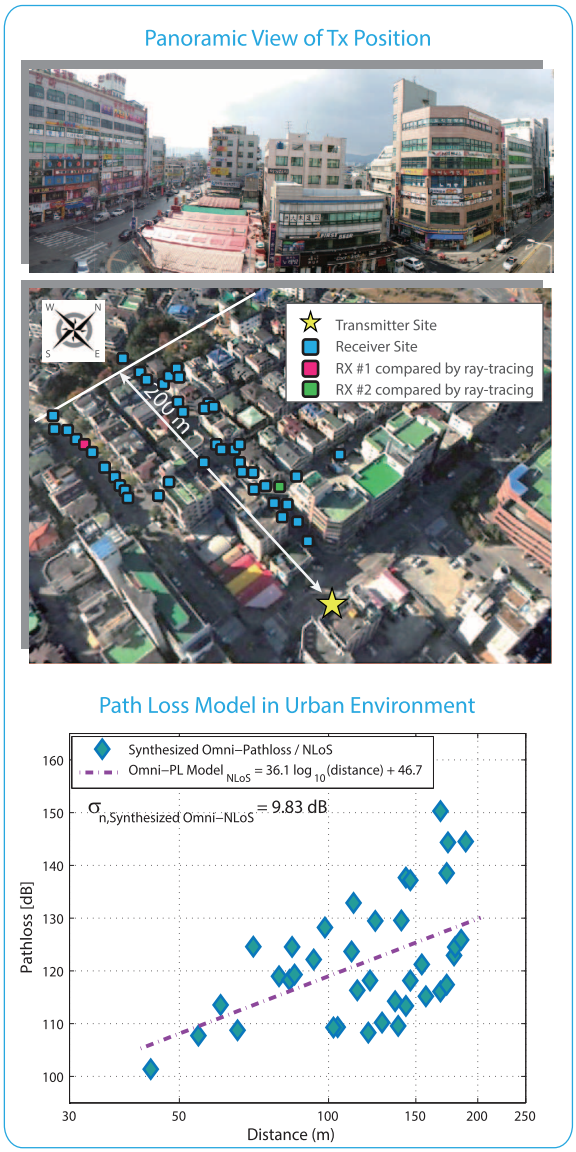


(a) Measurement in Urban Street-Canyon [6]

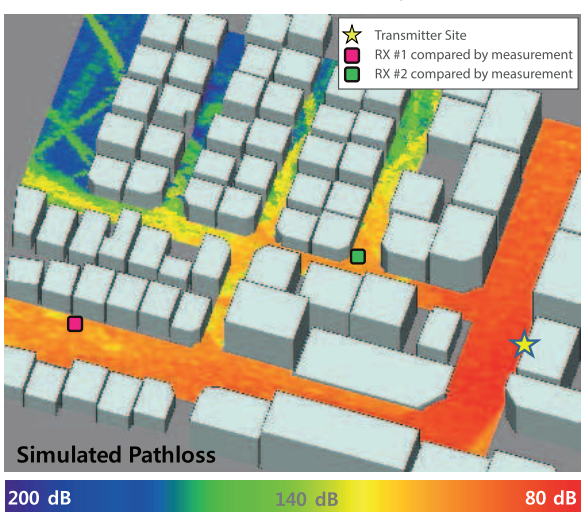


(b) 3D-Building Model and Ray-tracing Simulation

Fig. 2. Urban Environment in Daejeon, Korea.

above ground) also rotating in azimuth and elevation planes with 10° steps. In the campaign, the antenna scanning range in the azimuth and elevation domains were from −60° to 60° and −40° to 10°, respectively, on the Tx side at one-side of the building; these ranges were from 0° to 360° and −60° to 60°, respectively, on the Rx side. The antenna steering range was highly dependent on the measurement environment, and the scanning range was adjusted by pre-checking the existence of dominant and reflected paths first. During the measurement campaign, a total of 48 measurement location data sets were obtained at different RX locations; however, 38 location data sets from different RX sites were used as valid observations. The other ten location data sets were considered as outage in signal detection, similar to measurements reported in [18]. Detailed information of the measurement campaign is presented in [24]. In the same area, radio propagation was ray-traced using a three-dimensional (3D) site-specific environment database and 3D building data as shown in Fig. 2. The 3D-model was utilized for ray-tracing simulation and will be discussed in Section III. In the 3D ray-tracing simulation in Daejeon urban area, the TX was placed 15 m above the ground on the same building used in the measurement campaign (denoted with a star), and the RX locations were placed at mobile heights of 1.5 m above the ground on a 1 m × 1 m rectangular grid within a 200 m × 200 m area, only considering outdoor RX deployment if the grid location was not within a building.

### C. NYU Campus Measurement Campaign and Simulation

The 28 GHz channel propagation measurement campaigns [5], [18], [25] were conducted at the NYU campus in New York City, where 74 TX-RX outdoor location combinations were measured with a 400 Mcps broadband sliding correlator channel sounder equipped with a pair of 24.5 dBi (10.9 degrees azimuth half-power beamwidth) horn antennas at both the TX and RX. Three TX sites were chosen on building rooftops that ranged from 7 m to 17 m above ground shown as yellow circles in Fig. 3 (a). In total, signal was acquired at 26 TX-RX location combinations for T-R separations within 200 m, while the remaining tested TX-RX location combinations resulted in signal outages. The measurements provided 28 GHz directional and omni-directional path loss models [5], [25], as well as ultra-wideband statistical spatial channel models [18], [20], [37].

Using a similar approach as used for Daejeon, the physical environment of the NYU campus area was modeled for the purpose of ray-tracing verification and analysis of channel characteristics. In the 3D ray-tracing simulations, trees are modeled as vegetation with an average 40 dB loss and no reflection to account for Washington Square Park, a large open space area near the NYU Manhattan campus with many trees and vegetation as shown in Fig. 3 (b). Applying the simplified model for the trees in Washington Square Park, the vegetation area is modeled as a square area with 8 m height with an averaged 40 m width at 4 m above ground. Using a statistical vegetation loss

Authorized licensed use limited to: K & L Gates. Downloaded on October 21,2025 at 14:40:17 UTC from IEEE Xplore. Restrictions apply.

(a) Measurement in NYU Campus, Manhattan [5]

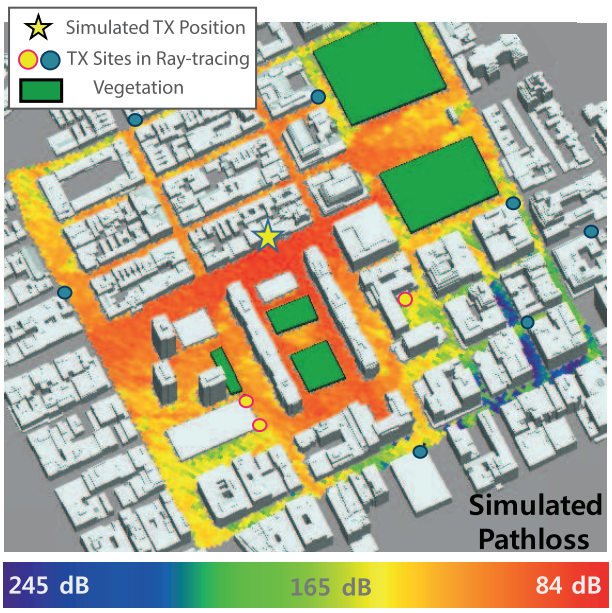


(b) 3D-Building Model and Ray-tracing Simulation

Fig. 3. Urban Environment in NYU Campus and 3D Building Model.

model [38], the average vegetation loss is assumed to be 40 dB with 40 m width penetration. It is also noted that no RX samples are simulated within the vegetation area to match the NYU measurements [5], [18]. To average out the site-specificity of the measurements and to remove the geometrical dependency of the statistical analysis, eight additional TX sites for the ray-tracer (marked as blue circles), as well as the same physical TX sites used in the NYC measurements [18] (marked as yellow circles), are used for the ray-tracing simulations. The area and the 3D-building models around the NYU campus, including the trees and eleven TX locations, are shown in Fig. 3 (b). The RX locations were placed at mobile heights of 1.5 m above the ground on a 5 m $\times$ 5 m rectangular grid within a 590 m $\times$ 450 m area, only considering outdoor RX deployment.

## III. Validation of Ray-Tracing Results

In this section, we describe details of the ray-tracing simulations, and validation procedures against the actual measurements.

### A. Ray-Tracing Simulations

The size and location of a study area are specified by the 3D model, which includes the terrain and building features. The ray-tracing simulation performs the method of shoot-and-bounce rays using the software tool, Wireless InSite [39]. The ray-tracer launches rays with $0.1^\circ$ angular spacing between rays. Some rays hit building walls, and then are reflected and continue to be traced up to the maximum number of reflections, diffractions, and penetrations. In our simulation settings, the ray-tracer accounts for up to 12 reflections, 2 penetrations, and 1 diffraction for each ray. For each multipath component (MPC), the ray-tracer accounts for the effects of reflection, diffraction, and penetration based on the geometrical optics (GO) and uniform theory of diffraction (UTD). The software evaluates the electromagnetic field according to the different rays received at RX location, and calculates propagation results in the form of received signal power, arrival delay, and departing/arrival angle information [39]. Full 3D ray-tracing is used, i.e., MPCs are not restricted to propagate just in a horizontal or vertical plane. On considering the mmWave propagation mechanisms in urban street canyon and to trace paths up to the maximum path loss, 250 dB as the minimum received power set by the ray-tracing software tool [39]. If any of the quantities for penetration, reflection, and diffraction reach their maximum number, or the power of a ray drops below the minimum traceable power, $-250$ dB, the ray is terminated on tracing. Due to the high computation of ray-tracing simulation, the numbers of reflections, penetrations, and diffractions were set to a manageable range without causing dramatic changes on simulation results. If all quantities of propagation mechanisms are small, the ray-tracing is not able to emulate all propagation effects, otherwise, the simulation requires extensive computation time. Multiple diffractions and more than two penetrations are ignored based on the high diffraction and penetration losses at 28 GHz [30], [31] and were not observed in preliminary runs of 28 GHz ray-tracing simulation. While 250 dB is clearly in excess of typical measurement ranges reported in the literature to date (typical values are 180 dB [18]), it offers some insights into the unknown. Future measurements should be performed to validate the ray-tracing results. This is further discussed in Sections IV and V.

The material properties are frequency-dependent [40], and the parameters of dielectric constant $\epsilon_r$ and conductivity $\sigma$ in the paper are estimated for the 28 GHz spectrum band based on the material properties in different bands [39], [41], [42]. The reference [41] provides the estimated material property values for 60 GHz, the values for 5.2 GHz are estimated in [42]. Using the frequency dependency of the property values, dielectric constant $\epsilon_r$ and conductivity $\sigma$, the parameters for 28 GHz used in the manuscript were linearly interpolated by the parameters on 5.2 GHz and 60 GHz. The buildings are assumed to be concrete with dielectric constant and conductivity of $\epsilon_r = 6.5$ and $\sigma = 0.668\,S/m$ at 28 GHz, respectively. The ground is modeled as wet earth with dielectric constant $\epsilon_r = 15$ and conductivity $\sigma = 1.336$S/m at 28 GHz, which are estimated for 28 GHz based on the values provided in the software tool in [39]. Linear interpolation might not be accurate; however, these

Authorized licensed use limited to: K & L Gates. Downloaded on October 21,2025 at 14:40:17 UTC from IEEE Xplore. Restrictions apply.

TABLE II
VERIFICATION OF MMWAVE NLOS CHANNEL CHARACTERISTICS

| | | Daejeon Measurement | Ray-Tracing |
|---|---|---|---|
| Delay Spread [ns] | E[DS] | 58.59 | 50.71 |
| | STD[DS] | 35.10 | 27.12 |
| Azimuth Angle Spread - Departure [deg] | E[ASD] | 8.53 | 4.41 |
| | STD[ASD] | 4.11 | 3.66 |
| Azimuth Angle Spread - Arrival [deg] | E[ASA] | 33.48 | 17.32 |
| | STD[ASA] | 14.67 | 13.98 |
| Zenith Angle Spread - Departure [deg] | E[ZSD] | 4.74 | 1.05 |
| | STD[ZSD] | 1.57 | 0.53 |
| Zenith Angle Spread - Arrival [deg] | E[ZSA] | 8.81 | 7.22 |
| | STD[ZSA] | 4.06 | 3.57 |

values are similar to the estimated values described in ITU-R P.2040 [40]. For simplicity scattering objects such as cars, people and street object (signs and billboard) are not considered. All buildings are modeled as planar surfaces (no window sills, door frames, etc.). Note that only outdoor points in the 3D geometry model are used for statistical analysis discussed in the later sections. In this section, the ray-tracing simulation performed for the purpose of validation is described only for the same RX locations as the measurements from the same TX sites, for proper comparison and validation of simulation and empirical results.

### B. Verification on 3D-Ray-Tracing Prediction in Daejeon

To verify the ray-tracing simulation in the Daejeon street-canyon environment, the statistical characteristics of the channels, such as delay and angular spreads, are compared. The root-mean-square (RMS) delay spread is calculated using the PDPs from both the measurement data [24] and the ray-tracing results. Only MPCs within 25 dB of the strongest component are taken into account. The angular spread is calculated by the method detailed in [34]. It is also noted that the beamwidth of the horn antenna poses a limit to the accuracy of our measurements and the analysis of the angular spread.

In Table II, the mean and standard deviation (STD) values of delay and angular spreads are calculated. Agreement between the ray-tracing and the measurement results is better for the delay spread than the angle spread. Fig. 4 shows the comparison between the Daejeon measurement campaign and the ray-tracing simulation on the cumulative density function (CDF) of the RMS delay spread and the azimuth spread of arrival (AoA). In the CDF of delay spread in Fig. 4 (a), a good agreement is observed for small delay spreads, though the prediction by ray-tracing yields smaller delay spreads than the measurements, most likely due to the fact that the simplified 3D-model ignores reflections from vehicles, small objects, and scattering that occurs in the measurements. For example, the power angular spectrum comparisons at two selected RX positions (RX 1, RX 2 in Fig. 2) are shown in Fig. 5. In each position, the LoS direction is shown. As seen from the geometry in Fig. 2 and these power spectra, most MPCs are traced in the simulations with similar normalized power level, except the paths at 0 degrees on RX 1 and 300 degrees on RX 2, which are reflected from small objects near those RX positions as measured in the field. Concerning the comparison of measured and

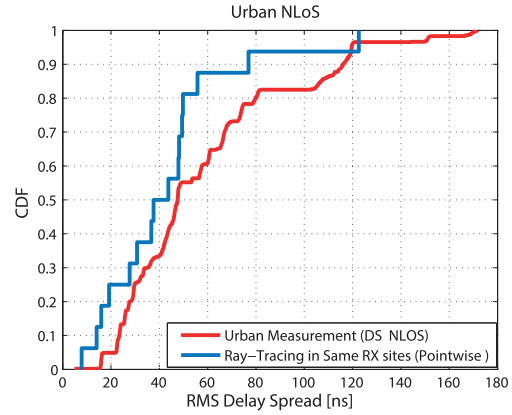


(a) Delay Spread

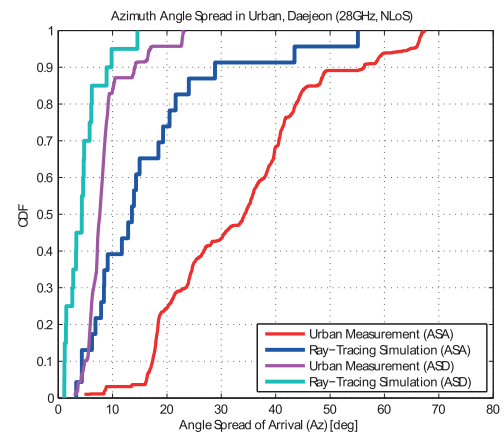


(b) Azimuth Angle Spread of arrival

Fig. 4. CDF Comparison between Measurements and Ray-tracing.

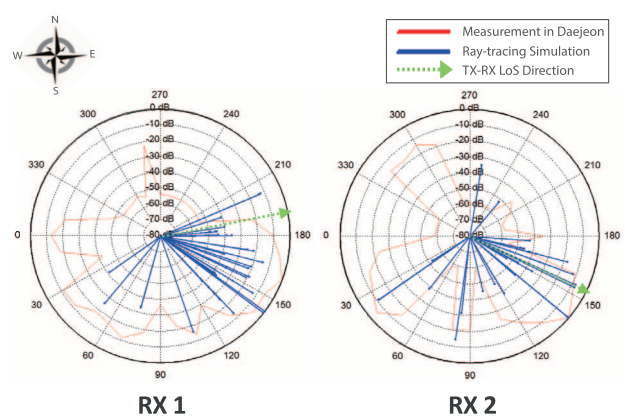


Fig. 5. Power-Angular Comparion between Raytracing and Measurement in Daejeon.

simulated angular spreads at the mobile station (AoA) in Fig. 4 (b), we conjecture that the reason for the considerable discrepancy lies in the simplified model of the environment that was used for the ray-tracing, and the lack of an accurate scattering ray tracing model [31]. Essentially, only flat building facades were modeled. However, reflections from street signs, lamp posts, parked cars, passing people, etc., could reach the RX from all directions, and would thus greatly increase the angular spread. At the same time, the "detour" distance of these

Authorized licensed use limited to: K & L Gates. Downloaded on October 21,2025 at 14:40:17 UTC from IEEE Xplore. Restrictions apply.

components would not be very large, since those scattering objects have to be close to the RX to reach appreciable power. Thus, the impact on the delay spread would be considerably smaller. Another possible explanation for the difference of the AoD angular spread lies in the extraction and modeling of the MPCs from the measurements with the horn antennas. In the angular spread of the measurement data, the angular pattern is removed in that all associated MPCs extracted in an angular "bin", are marked as being from the center angle of this bin. This to a certain degree avoids the "smearing out" of the angular power spectrum that one normally would observe with Bartlett beamformers. However, on the downside, this approach leads to an *under*estimation of the overall angular spread, because rays with slightly different angles are artificially forced into the same AoA (and AoD).

Scattering is widely considered as a critical propagation mechanism in the mmWave band [7], [18], [31], and ray-tracing accuracy improves when modeling of scattering effects is included. However, some recent work claimed that the scattering effect in ray-tracing is not always influential for mmWave channel characteristics [28]. Still, the back-scattering from objects in the street and micro-objects such as window frames play an important role [43], [44]. We also observe similar results from the comparison between the ray-tracing simulation and the Daejeon measurements as shown in Fig. 5. The scattering effect in mmWave band is still in open area to be investigated more, however, some results point out that the scattering could be affected less in outdoor long distance propagation because the small amount of energy is propagated through scattering in outdoor long-distance propagation channels. Even with the limitation of ray-tracing models without the micro-object modeling or scattering, the results on ray-tracing show the ability to predict the large-scale channel characteristics in 28 GHz band.

### *C. Verification of 3D-Ray-Tracing Prediction With NYU Campus Measurements*

A similar verification between the measurements and the ray-tracing simulations in the NYU Campus area is performed. Due to the limited empirical dataset in [5], azimuth angular spread of arrival (ASA) at non-line-of-sight (NLoS) RX sites and path loss model are compared in Fig. 6. The mean and STD values of the azimuth ASA is summarized in Table III. The angle spread comparison shows that the ray-tracing results are similar to the measurement like the comparison in the Daejeon street-canyon. Furthermore, the 28 GHz path loss is compared in Fig. 6, showing reasonable agreement between the simulation and measurements. For fair comparison between the measurement and the ray-tracing results, only the data obtained in the TX locations marked with yellow circles in Fig. 3 were used. It must be noted that T-R separation distances of physically measured TX-RX locations were obtained from maps by NYU WIRELESS, computed using the $(x, y, z)$ coordinates of TX and RX locations in our simulations, which introduces slight differences of distance on the pointwise comparison from the data in [18]. In ray-tracing simulation, it is very hard to exactly model the TX and RX locations of the measurement campaign

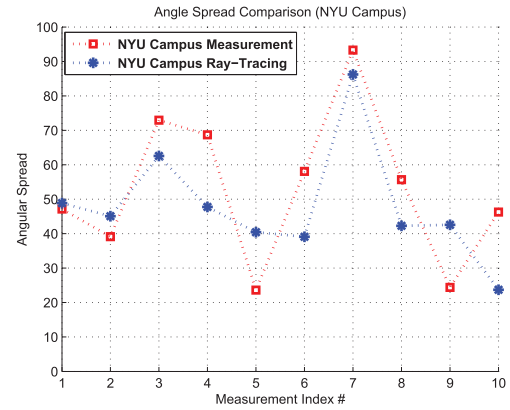


(a) RX Angular Spread

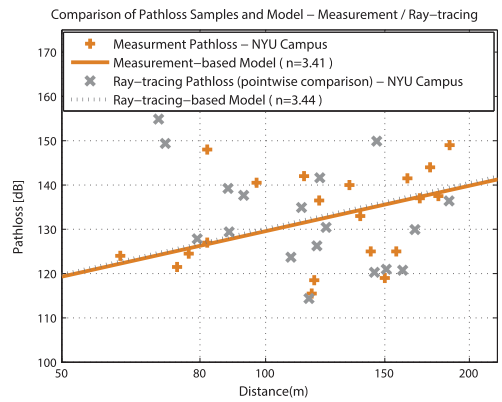


(b) path loss Model

Fig. 6. Comparison of NYU Measurement and Ray-tracing.

TABLE III
COMPARISON OF NYU MEASUREMENT AND RAY-TRACING

| | NYU Measurement | 3D Ray-Tracing |
|---|---|---|
| Mean of Az. Angle Spread of Arrival [deg] | 52.93 | 47.85 |
| STD of Az. Angle Spread of Arrival [deg] | 21.74 | 16.57 |

and to pick them on the 3D map precisely. We derived the path loss model based on the ray-tracing simulations in Fig. 6. Note that these models are derived using the close-in reference distance model for fair comparison. The ray-tracing based models are compared with the previous NYU measurement-based path loss model [18], [25]. The pointwise comparison between the measurement and ray-tracing simulations shows considerable deviations. However, the path loss models derived from these values show reasonable agreement. This is an effect commonly observed in ray tracing, and could only be eliminated by a much more detailed database including small-objects in street as discussed in the comparison on Daejeon previously. On the other hand, the details of building structures in NYU area are modeled in 3D, which can induce back-scattering from the building surface, leading to a good agreement between the ray-tracing and the measurement data in comparison of angular spread. This verification suggests that scattering and reflections

Authorized licensed use limited to: K & L Gates. Downloaded on October 21,2025 at 14:40:17 UTC from IEEE Xplore. Restrictions apply.

from small objects affect the mmWave propagation channel, however, they are not as important as major specular scatterers or reflectors in urban outdoor environments, similarly to the results in [29].

## IV. mmWave Channel Propagation Model in Urban Environment

Most standardized channel models like 3D-SCM, WINNER II, and ITU models [33], [34], [35] are based on double-directional channel models [45]. Furthermore, all these models adopt the concept of clusters, where the properties of the clusters such as cluster angular spreads are modeled as random variables. These random variables (referred as large-scale parameters, LSPs) are correlated with other LSPs, e.g., channel angular and delay spreads and shadowing, are typically modeled as correlated lognormally distributed random variables. Using the generated LSPs for each user, multiple MPCs are generated for each cluster with properties determined by the realizations of the LSPs.

Similar to the concept of clusters, in [25], spatial lobe characteristics were studied for mmWave band, where a spatial lobe was defined to be a contiguous spread of received power in azimuth and/or elevation at the TX or RX, and corresponding to a main angle of arrival or angle of departure at which energy is prominent. As directional transmissions and receptions are expected to drive mmWave systems, it is important to capture spatial lobe properties that can be used to gain insight into proper beamforming and beamcombining algorithms for radio system design. Thus, the concept of cluster or spatial lobe holds an important role for mmWave communication systems, and the mmWave channel model in [20] follows a 3GPP 3D-SCM-like modeling approach.

We next derive propagation models based on the verified ray-tracing simulations. First, the path loss model including shadowing factor and line-of-sight (LoS) probability is analyzed. Then, the set of LSPs for generating multipath components with small-scale parameters are extracted for channel modeling. With the help of the ray-tracing results, all channel model parameters following the system-level approach [33] are derived, because some parameters were not easily derived from the measurement analysis, especially parameters for LoS condition which had fewer measurement locations. We derived the channel model based on the calibrated ray-tracing simulations, and compare the channel model with measurements and the ray-tracing.

In this paper, we propose a channel propagation model for three scenarios: Daejeon, NYU urban microcell (UMi), and NYU urban macrocell (UMa). The Daejeon scenario corresponds to the UMi, especially street-canyon environment. The ray-tracing models for Daejeon and NYU in Sections II and III are reused in this section. In order to obtain a sufficient number of measurement samples for the reliable channel propagation modeling, channel impulse response (CIR) data are collected with 1 m and 5 m resolution of RX locations for the Daejeon and NYU models, respectively. The TX height of Daejeon model is set to 16 m for one TX site. In the NYU model, we consider two TX installation scenarios according to their heights, in each with 11 TX sites for each case. In NYU UMa, the TX is placed 5 m above the rooftop (where the rooftop heights are explained in [18]), whereas the height of the TX is 10 m from the ground in NYU UMi.

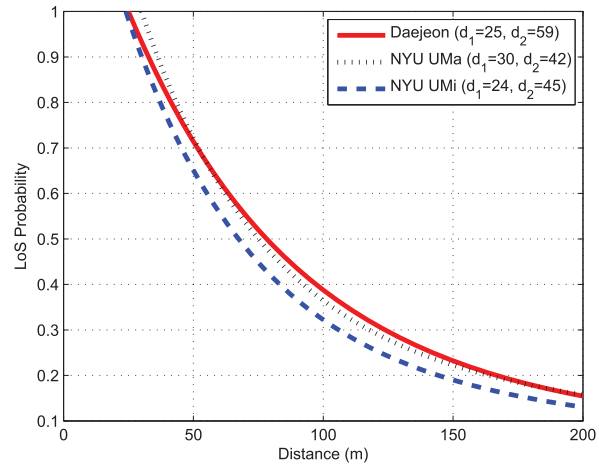


Fig. 7. LoS Probability Model of Daejeon and NYU Campus, for Urban Micro and Urban Macro.

### A. LoS Probability

The LoS probability defines how often there exists a direct (optical) path for a TX-RX pair.

The LoS probability is a basic feature of channel modeling since the propagation characteristics vary considerably with existence of LoS. For system evaluations, the LoS probability function is modeled as an exponential function of distance $d$ with two parameters $d_1$ and $d_2$ as follows [35]:

$$P_{LoS}(d) = \min(d_1/d, 1)\,(1 - \exp(d/d_2)) + \exp(d/d_2) \quad (1)$$

where $d$ is the 2D distance in meters between TX and RX, and $d_1$ and $d_2$ are scenario parameters optimized to fit a set of ray-tracing data. We obtain the LoS probability by ray-tracing. We separately calculate the LoS probabilities of Daejeon, UMi NYU and UMa NYU scenarios, and fit parameters $d_1$ and $d_2$ according to a minimum RMS criterion. A similar analysis using the NYC environment was performed in [46], showing a slightly modified LOS probability equation with a 'square' exponent, yielding a smaller minimum mean square error than (1).

The LoS probability function and its parameters $d_1$ and $d_2$ for each scenario are depicted in Fig. 7. In the NYU simulations, the UMa scenario has 3-10 percent higher LoS probability than UMi for all distances as expected. $d_1$ of UMa is greater than that of UMi due to the different TX installation heights, which causes varying 3D distances for different scenarios at the same RX location. Also, the UMa scenario has higher probability for the LoS path to reach an RX point behind buildings. This implies that the LoS probability increases with TX height. In the Daejeon scenario with 16 m TX height, $d_1$ is calculated as 25 m, which is similar to NYU UMi case. However, it is observed that the LoS probability in Daejeon scenario looks similar to NYU UMa scenario for the 40-200 m distance range.

Authorized licensed use limited to: K & L Gates. Downloaded on October 21,2025 at 14:40:17 UTC from IEEE Xplore. Restrictions apply.

TABLE IV
LARGE-SCALE PARAMETERS IN PATH LOSS AND SHADOW FADING MODEL

| | | UMi | | | | UMa | |
|---|---|---|---|---|---|---|---|
| | | Daejeon | | NYU Campus | | NYU Campus | |
| | | LoS | NLoS | LoS | NLoS | LoS | NLoS |
| CI | $\overline{n}$ | 1.90 | 3.15 | 1.81 | 3.03 | 1.87 | 2.97 |
| | $\sigma_{\text{CI}}$ [dB] | 0.63 | 22.09 | 2.05 | 17.99 | 1.74 | 15.92 |
| | Valid Range | up to 200m | | up to 200m | | up to 200m | |
| FI | $\alpha$ | 1.76 | 5.69 | 1.28 | 3.55 | 1.67 | 3.39 |
| | $\beta$ | 64.22 | 10.31 | 72.25 | 50.88 | 65.40 | 52.74 |
| | $\sigma_{\text{FI}}$ [dB] | 0.57 | 20.74 | 1.89 | 17.91 | 1.70 | 15.86 |
| | Valid Range | up to 200m | | up to 200m | | up to 200m | |
| Dual | $d_{\text{th}}$ | N/A | 80m | N/A | 150m | N/A | 150m |
| | $\alpha_1$ | | 0.76 | | 2.57 | | 2.42 |
| | $\alpha_2$ | | 10.73 | | 11.04 | | 9.75 |
| | $\beta_1$ | | 92.79 | | 68.55 | | 70.94 |
| | $\sigma_{\text{FI}}$ [dB] | | 19.65 | | 23.76 | | 21.03 |
| | Valid Range | | up to 200m | | up to 400m | | up to 400m |

Comparisons between Daejeon and NYU thus show that the LoS probability highly depends on the geometry of the site in which the experiment is conducted.

### *B. Large-Scale Fading Model : Path Loss and Shadow Fading*

In deriving LSPs such as path loss and shadow fading, the total power that aggregated all the detected rays' power in the linear scale was used. We propose three types of path loss models: the close-in free space reference distance (CI) model [47], the floating intercept (FI) model [34] and the dual-slope model [2], [21], [48]. The CI path loss is the simplest model determined only by one path loss exponent (PLE) $\overline{n}$. The CI path loss model at distance $d$ is written as follows:

$$\text{PL}_{\text{CI}}(d) = \text{PL}_{\text{FS}}(d_0) + 10\overline{n}\log_{10}(d/d_0) + \mathbf{x}_{\sigma_{\text{CI}}} \qquad (d \geq d_0) \tag{2}$$

where $d_0$ and $\text{PL}_{\text{FS}}(d_0)$ are the reference distance and free-space path loss at the reference distance by the Friis' free-space equation, respectively. The deviation of path loss is modeled as random variable $\mathbf{x}_{\sigma_{\text{CI}}}$ following log-normal distribution with standard deviation $\sigma_{\text{CI}}$. We set $d_0$ to 1 m in our CI path loss results [37]. The FI path loss model eliminates the assumption of free-space path loss at the reference distance. Instead, the FI path loss model with standard deviation $\mathbf{x}_{\sigma_{\text{FI}}}$ is determined by two parameters: slope $\alpha$ and intercept $\beta$ which is estimated by least-squares linear regression, as follows:

$$\text{PL}_{\text{FI}}(d) = 10\alpha\log_{10}(d) + \beta + \mathbf{x}_{\sigma_{\text{FI}}}. \tag{3}$$

On modeling of path loss from data sets, the selection of valid samples for models is important which can regenerate the data sets within valid samples through the models. Considering both the CI and FI path loss models, the ray-tracing data samples up to 200 m distance range are used for estimating both models, which distance range is set to match the maximum distance of measurement campaigns introduced in Section II and and calibrated between measurement campaigns and ray-tracing simulations in Section III. The CI and FI models are derived and the parameters of path loss models are summarized in Table IV with the valid range of each model. However, although the majority of users will be placed within 200 m range using mmWave cellular services, an appropriate extrapolation method over the valid distance from the measurement campaign is required to model interferences from other transmitters in adjacent cells over 200 m distance range [33], [35]. It is noted that in order to avoid a parameter estimation bias due to the different number of channel samples over distance in ray-tracing, the local mean path loss values are used for estimating the channel model parameters [48]. It is also utilized for representing the change of mean values of path loss scatters.

Both CI and FI path loss models are classified as single-slope path loss models. These are well-fitted when the observation area is small enough to have similar propagation characteristics. However, the single-slope path loss sometimes has large RMS error between the model and local mean path loss samples, especially, large distance range in NLoS environments [48] caused by the high diffraction loss and multiple reflection effects at building corners in NLoS. Since large errors do not represent mean path loss values well, a dual-slope path loss model [48] was proposed to represent the propagation phenomenon as the distance becomes large, especially in NLoS environments. In the proposed dual-slope model, the ray-tracing data is used for extrapolating the path loss model up to 400 m distance range. It would be a useful data to model the long-distance range based on ray-tracing data. In the dual-slope model, the second slope is the same as the CI model which has an anchor point on the end of the first slope; only the first slope is adapted for the FI path loss model derived by linear regression. This dual-slope model derived in this approach provides the small RMS error between path loss and model in the first slope and the second slope over all distance range (note the dual-slope CI equation is not shown for convenience, see [21], [47], [49]). The dual-slope path loss equation with standard deviation $\mathbf{x}_{\sigma_{\text{dual}}}$ is a continuous equation composed of two slopes $\alpha_1$ and $\alpha_2$, intercept $\beta_1$, and threshold distance $d_{\text{th}}$ as follows:

$$\text{PL}_{\text{Dual}}(d) = \begin{cases} \beta_1 + 10\alpha_1\log_{10}(d) + \mathbf{x}_{\sigma_{\text{dual}}} & \text{for} \quad d \leq d_{\text{th}} \\ \beta_1 + 10\alpha_1\log_{10}(d_{\text{th}}) + 10\alpha_2\log_{10}(d/d_{\text{th}}) + \mathbf{x}_{\sigma_{\text{dual}}} & \\ \qquad\qquad \text{for} \quad d > d_{\text{th}}. & \end{cases} \tag{4}$$

For the dual-slope path loss case which is predicted for larger distances $(> 200m)$ than single-slope cases, the maximum distance between TX and RX is set to 400m. The threshold distance $d_{\text{th}}$ is determined optimally to minimize the RMS error between estimated dual-slope path loss formula and local mean path loss. In this paper, we assume that $d_{\text{th}}$ is a multiple of 10 m increments for computational convenience. Table IV lists the parameters of three types of path loss equations and the corresponding STD of shadow fading. Fig. 8 shows the scatter plot of path loss samples, CI, FI and dual-slope path loss equations and their corresponding slopes.

In LoS environments, the single-slope path loss equation is well-matched to the path loss samples. The PLE in the CI model ranges from 1.81 to 1.90 and the slope of the floating-intercept path loss fits from 1.28 to 1.76. Note that all of them are less than 2 due to the ground reflection and other MPCs, which occur *in addition to* the LoS; this could also be interpreted as a waveguiding effect due to street canyons. The STD $\sigma$ of shadow fading is very small. In the NLoS environments, the

Authorized licensed use limited to: K & L Gates. Downloaded on October 21,2025 at 14:40:17 UTC from IEEE Xplore. Restrictions apply.

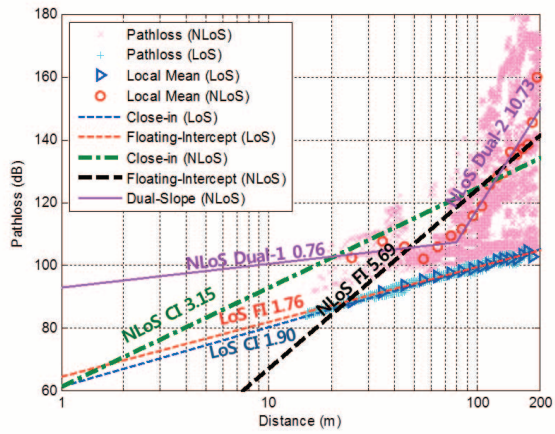


(a) Daejeon

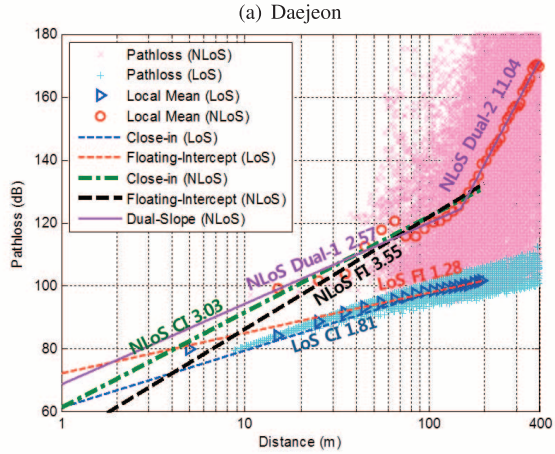


(b) NYU UMi

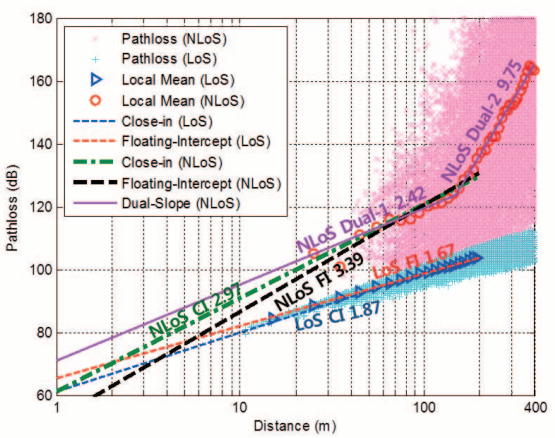


(c) NYU UMa

Fig. 8. Path loss equations and slopes.

PLE $\overline{n}$ have a value close to 3, which is not large compared with PLEs observed in currently used in cellular communication systems [34]. The slope $\alpha$ for FI varies from 3.39 in NYU UMa to 5.69 in Daejeon. These results show that the FI path loss model is more sensitive to the geometrical environments than the CI path loss model. The appropriateness of the dual-slope feature is clearly shown in all cases, although the STD between all three models are not significantly different from each other (differences are generally less than an order of magnitude of the STD of any model). The standard deviation of shadow fading in NLoS is large, ranging from 15.86 dB to 23.76 dB, which is caused by the huge shadowing losses at mmWave as predicted by the ray tracer with up to 250 dB range. In the ray-tracing simulation we conducted, all samples are located in the area with 1 m / 5 m grid locations, which represents the locations of deep shadow NLoS points and the locations of NLoS points close to near LoS points with small additional loss induced from LoS path loss. The ray-tracing results in Fig. 2 (b) and Fig. 3 (b) also show no abrupt boundary between LoS and NLoS transition, however, the results are categorized to LoS and NLoS conditions by visual inspection on the existence of LoS path. These path loss samples are plotted in the scatter plot in Fig. 8, and the big differences between NLoS path loss in deep-shadowed area and NLoS path loss in near LoS can cause large variance of path loss, i.e., large SF (shadow fading). The large variance of path loss at 28 GHz is induced from the mmWave propagation characteristics which is mainly propagated by the reflection and diffraction with higher loss than at lower frequencies without penetration of buildings and with ray tracing scattering models that may not capture all of the actual channel energy [31]. Another aspect of the large variance of path loss model is that the path loss on ray-tracing has much greater level of sensitivity than the limit of practical wideband channel sounders. Generally, the choice of the sensitivity limit can have an important impact on the overall channel model. Discarding any points with a path loss above a threshold $T$ has both advantages and drawbacks: the advantage is that points with very high path loss are of dubious physical reality, since such low power points cannot be easily verified by measurements or deployed systems [31], [50]. On the other hand, picking a small $T$ creates a "selection bias", since then the path loss law would only be fitted to the low-path loss points. For very large distances where signals are weaker, only a few points (all of them close to $T$) would be selected for the model fitting, so that the path loss fit in that range would become highly compressed at the cut-off level. Alternatively, the errors induced from the truncated data can be compensated by Maximum-likekihood estimation in path loss model parameters [52]. In this work, the ray tracer was allowed to have a much larger measurement range than all available measurements in order to explore unknown effects. Recently, many measurement-based results [49], [51] are being published to propose single-slope path loss model, and more measurements with greater range are needed to corroborate ray tracing results at very large path loss values (greater than available measurement ranges of of 180 dB).

The averaged shadow fading over all distance ranges is modeled with large values. To derive a geometry-induced shadow fading, the shadow fading value is analyzed as a function of distance. In Fig. 9, the local STD of shadow fading and its fitted linear model of shadow fading are presented. Linear regression is performed by minimizing the MSE of the model with local shadow fading. In the LoS environment, the STD of shadow fading stays small. Thus, a value $\sigma$ that is constant over distance is sufficient to capture the shadow effects in LoS. In contrast to LoS, the STD in NLoS remarkably increases with distance due to the large blockage losses at mmWave frequencies. Thus, a linear shadow fading function over distance is more appropriate for modeling NLoS shadow fading.

Authorized licensed use limited to: K & L Gates. Downloaded on October 21,2025 at 14:40:17 UTC from IEEE Xplore. Restrictions apply.

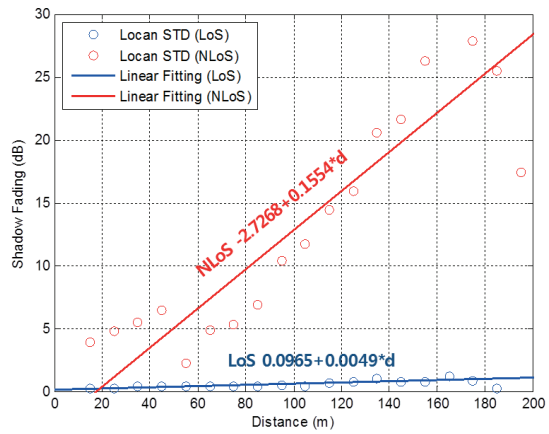


(a) Daejeon

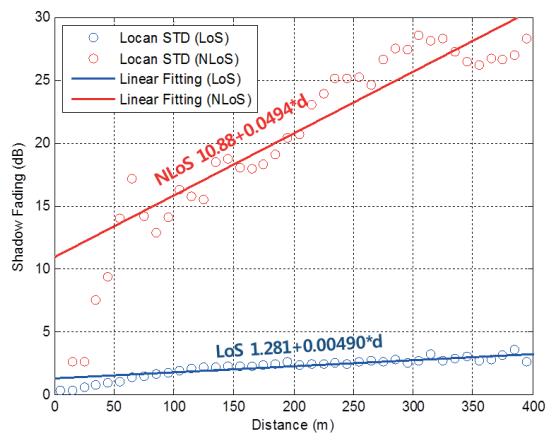


(b) NYU UMi

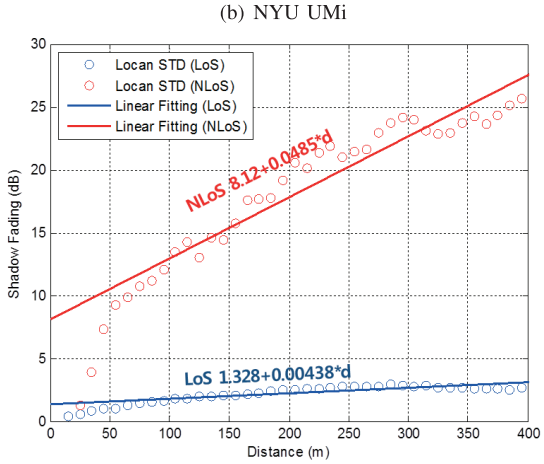


(c) NYU UMa

Fig. 9. Standard deviation of shadow fading versus distance.

### C. Small-Scale Fading in Spatio-Temporal Channel Model

The channel parameters in delay and angular domains were extracted from the ray tracing results. The values of delay spread in the 28 GHz band are smaller than the values of delay spread in the conventional cellular band. This is mainly caused by the propagation characteristic of the mmWave band that undergoes less specular reflection and more scattering [18], [31], and where paths that involve multiple diffractions and penetrations are more strongly attenuated. Besides the parameters shown in Table V, it is verified that the excess delays at both 28 GHz are exponentially distributed, and azimuth angle of departure (AoD) and azimuth angle of arrival (AoA) follow a Laplacian distribution as reported previously [1]. For cluster-wise analysis, the K-Power-Means algorithm [53] is utilized for clustering of observed MPCs. This algorithm is iterative and uses a distance metric based on the power-weighted multipath component distance (MCD). The algorithm minimizes the sum of MCDs between each MPC in the cluster to their centroid, which has the effect of minimizing cluster angular and delay spreads. Note that the delay scaling factor in the MCD is set to 5 and the Kim-Park (KP) index proposed in [54] is used for determining the optimum number of clusters, following the approach in [55]. After the clustering, the results from the ray-tracing simulations are analyzed in the spatio-temporal domain, for cluster parameters such as delays, angles at the TX and RX, and received powers. Based on the observed clusters in each link, LSPs such as inter-cluster and intra-cluster delay spreads and angle spreads are analyzed using the framework in [34]. For further modeling purpose, the 28 GHz channel parameters of the fitted distributions for the LSPs, such as $(\mu, \sigma)$ for the log-normal distribution and $1/\lambda$ for the exponential distribution, are summarized in Table V.

In the 3D extension of the channel model, the elevation angle spread at TX, which is also referred to as zenith angle spread departure (ZSD), is analyzed and modeled by an exponential distribution. Following the 3GPP 3D-channel model [33], the statistics of elevation angle are modeled as a function of distance between TX and RX. In Fig. 10 (a), each ZSD is plotted as scatter point and their local mean and STD are plotted overlaid as red and magenta dotted line; they clearly depend on distance. The modeling of distance-dependency for the mean and the STD of ZSD follows the one in [33] with a breakpoint in a single-slope and a constant value. However, it is observed that the mean and the STD of ZSD still have a distance-dependency that decreases as TX-RX distance increases. The modified model with the dual-slope is proposed as shown in Fig. 10 (a) where the parameter $1/\lambda$ represents the model. The zenith angle spread arrival (ZSA) follows the model in [33] exhibiting a log-normal distribution with the parameters in Table V. The offsets of elevation angles, i.e., the local mean of elevation angles, zenith of departure (ZoD) and zenith of arrival (ZoA), are also modeled as a distance-dependent function as shown in Fig. 10 (b). The offset of ZoD is well matched to the channel model in [33], however, we propose to model the offset of ZoA in a different manner from [33] by a power function, because the ZoA offset should be modeled as lower than zero in the far region. In that range, a LoS path exhibits only a very small offset above, and most paths are coming from the ground-level. The proposed fitted models are plotted in Fig. 10 (b). The parameters for elevation angle spread models and angle offset models are described in the later channel modeling section.

## V. Channel Modeling

In this section, the ray-tracing-based mmWave channel models for UMi and UMa scenarios are proposed. The procedures

Authorized licensed use limited to: K & L Gates. Downloaded on October 21,2025 at 14:40:17 UTC from IEEE Xplore. Restrictions apply.

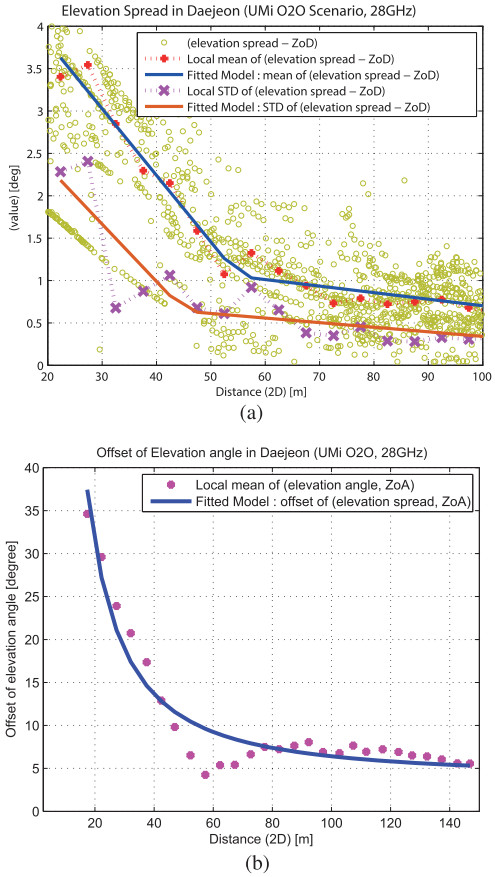


Fig. 10. Elevation Angle Spread and Angle Offset in 3D Channel Model (a) Zenith spread at departure (ZSD) and dual-sloped (b) Elevation angle offset and the fitted-model of offset.

for generating channel realizations are similar to the standardized channel model in [12], to which some modifications from the observations in the previous section are suggested.

### A. Generation of Channel Parameters

In this subsection, the channel generation methodology is presented based on the obtained parameters in the previous section. After applying the path loss model, $N$ clusters, path delays, path AoD/AoA and ZoD/ZoA are generated. Then, with the generated spatio-temporal channel parameters of clusters and paths, one can compute the channel coefficients for each cluster and each TX-RX antenna pair, $\mathbf{H}_{u;s;n}(t)$ which is defined in [33]. The generation procedures of each channel parameter are described later in this section, and the channel LSPs are randomly generated according to the distribution and parameters summarized in Table V. For a more realistic channel model that reflects measurements, the number of clusters $N$ should be generated as a realization of a random variable following a Poisson distribution. However, due to the complexity of the channel model and the difficulty of deriving all conditional probabilities of relevant channel parameters, we instead use a fixed number of clusters, $N$ = 6, for simplified channel modeling. In this section, we follow the convention of 3GPP type models to call a "cluster" a "path", and an "MPC" is called a "subpath". The number of subpaths is set to 20 in the 3GPP 3D-channel model and ITU channel model in legacy bands below 6 GHz, however, the number of subpaths is smaller in the mmWave band according to the ray-tracing observation and has been observed to range from just a few, but rarely to as many as 30 subpaths [20]. The limited number of paths in ray-tracing reinforces the observation of smaller number of subpaths in mmWave band because much smaller number of paths, such as one or a few paths, can be observed as a cluster in the far distance or in severely deep shadowed region than in the legacy bands. For simplicity of the modeling, the number of subpaths $M$ is also fixed to 10 in the proposed model. The large-scale parameters are randomly generated according to log-normal distributions, whose parameters are correlated with each other [35]. The correlation coefficients are summarized in Table V. The cross-correlation is a channel parameter which indicates the similarity and dependence of two channel parameters where the value of cross-correlation ranges between $-1$ to 1. For example, a cross-correlation value of 1 means that that two channel parameters behave identically in a statistical sense whereas a correlation value of 0 means that there is no correlation between them. In both system-level and link-level simulations, the cross-correlation coefficient between channel parameters is used to generate correlated LSPs used in the spatial wireless channel in ITU channel model [35] or 3GPP channel model [33], and provide a similar propagation conditions in the spatial domain [56].

**Path delays**: The delay spread $\sigma_{\text{DS}}$ is modeled as an exponential random variable with mean $\lambda$ in Table V. Then, the $n$-th cluster delay is generated via an auxiliary realization of exponential random variables as [35] $\tau'_n = -r_{\text{DS}}\sigma_{\text{DS}} \ln(X_n)$ where $r_{\text{DS}}$ is the delay distribution proportionality factor, $X_n \sim \mathcal{U}(0,1)$, and the cluster index $n = 1, \cdots, N$. The cluster delay $\tau_n$ is then calculated by normalization and descending sorting, $\tau_n = \text{sort}\left(\tau'_n - \min\left(\tau'_n\right)\right)$. The subpath delays $\tau_{n,m}$ are calculated by adding the intra-cluster delay offset. Even though the intra cluster delay spread is obtained from the ray-tracing results, we simply added the fixed delay offset, similarly to the ITU model. The delays of the subpaths are grouped and defined by

$$\begin{aligned}\tau_{n,m} =& \tau_n + 0\ [\text{ns}], \quad m = 1,2,3,4,10\\ \tau_{n,m} =& \tau_n + 5\ [\text{ns}], \quad m = 5,6,9\\ \tau_{n,m} =& \tau_n + 10\ [\text{ns}], \quad m = 7,8\end{aligned}$$

**Path powers** : Cluster powers are modeled as exponential distribution, and the cluster powers are related to the exponentially distributed cluster delays. Determine first

$$P'_n = \exp\left(-\tau_n \frac{r_{\text{DS}} - 1}{r_{\text{DS}}\sigma_{\text{DS}}}\right) \cdot 10^{\frac{-\mathbf{Z}_n}{10}} \tag{5}$$

where $\mathbf{Z}_n \sim N(0,\xi)$ is the inter-cluster shadowing factor in [dB]. Then, the cluster power of each channel realization is normalized, and expressed as

$$P_n = \frac{P'_n}{\sum_{n=1}^{N} P'_n}. \tag{6}$$

Authorized licensed use limited to: K & L Gates. Downloaded on October 21,2025 at 14:40:17 UTC from IEEE Xplore. Restrictions apply.

TABLE V
CHANNEL MODEL PARAMETERS

| Scenario | | UMi | | | | UMa | |
|---|---|---|---|---|---|---|---|
| Environment | | Daejeon | | NYU Campus | | NYU Campus | |
| | | LoS | NLoS | LoS | NLoS | LoS | NLoS |
| log(DS[s]) | $\mu_{\text{DS}}$ | -7.67 | -7.31 | -7.05 | -6.91 | -6.97 | -6.80 |
| | $\sigma_{\text{DS}}$ | 0.30 | 0.60 | 0.44 | 0.54 | 0.50 | 0.72 |
| log(ASD[°]) | $\mu_{\text{ASD}}$ | 1.15 | 0.82 | 1.18 | 0.94 | 1.07 | 1.21 |
| | $\sigma_{\text{ASD}}$ | 0.46 | 0.42 | 0.47 | 0.66 | 0.54 | 0.68 |
| log(ASA[°]) | $\mu_{\text{ASA}}$ | 1.23 | 1.35 | 1.51 | 1.48 | 1.49 | 1.51 |
| | $\sigma_{\text{ASA}}$ | 0.34 | 0.42 | 0.27 | 0.43 | 0.38 | 0.42 |
| log(ZSA[°]) | $\mu_{\text{ZSA}}$ | 0.61 | 0.59 | 0.59 | 0.34 | 0.66 | 0.53 |
| | $\sigma_{\text{ZSA}}$ | 0.51 | 0.40 | 0.22 | 0.35 | 0.36 | 0.37 |
| E[ZSD[°]] | $\gamma_1$ | -0.109 | -0.093 | -0.037 | -0.041 | -0.039 | -0.251 |
| | $\eta_1$ | -6.288 | 6.062 | 2.215 | 2.52 | 3.463 | 11.7 |
| | $\gamma_2$ | -0.010 | -0.007 | -0.002 | -0.002 | -0.008 | -0.002 |
| | $\eta_2$ | 1.37 | 1.466 | 0.647 | 0.82 | 1.767 | 1.254 |
| ZoD Offset[°] | $a_{\text{ZoD}}$ | -∞ | -0.978 | -∞ | -1.53 | -∞ | -0.946 |
| | $b_{\text{ZoD}}$ | 0 | 30 | 0 | 30 | 0 | 30 |
| | $c_{\text{ZoD}}$ | | 2.314 | | 3.37 | | 2.778 |
| ZoA Offset[°] | $a_{\text{ZoA}}$ | 0 | 167.73 | 0 | 867.81 | 0 | -15.50 |
| | $b_{\text{ZoA}}$ | | -0.47 | | -1.14 | | 0.30 |
| | $c_{\text{ZoA}}$ | | -12.91 | | 0.21 | | 69.74 |
| Delay Distribution | | Exponential | | | | | |
| AoD/AoA Distribution | | Wrapped Gaussian | | | | | |
| ZoD/ZoA Distribution | | Laplacian | | | | | |
| $r_{\text{DS}}$ | | 2.82 | 2.06 | 2.62 | 2.10 | 2.78 | 1.98 |
| $K$-factor $(K)$ $[dB]$ | $\mu$ | 8.54 | N/A | 6.82 | N/A | 7.00 | N/A |
| | $\sigma$ | 6.57 | N/A | 6.96 | N/A | 6.84 | N/A |
| $N$ | | 6 | 6 | 6 | 6 | 6 | 6 |
| $M$ | | 10 | 10 | 10 | 10 | 10 | 10 |
| Cluster ASD [°] | | 2.7 | 5.7 | 2.5 | 2.9 | 1.9 | 4.8 |
| Cluster ASA [°] | | 3.3 | 6.7 | 2.9 | 3.5 | 2.7 | 6.8 |
| Cluster ZSD [°] | | 1.2 | 1.6 | 0.4 | 1.6 | 1.0 | 2.2 |
| Cluster ZSA [°] | | 3.9 | 4.9 | 1.7 | 8.3 | 3.4 | 6.4 |
| ASD vs DS | | -0.25 | 0.37 | 0.31 | 0.41 | 0.20 | 0.45 |
| ASA vs DS | | 0.35 | 0.43 | 0.17 | 0.23 | 0.30 | 0.33 |
| ASA vs SF | | -0.01 | 0.03 | 0.19 | -0.17 | 0.15 | 0.07 |
| ASD vs SF | | -0.24 | 0.16 | -0.01 | 0.17 | -0.06 | 0.26 |
| DS vs SF | | 0.22 | 0.30 | -0.03 | 0.18 | 0.05 | 0.31 |
| ASD vs ASA | | -0.67 | 0.09 | -0.15 | 0.18 | 0 | 0.29 |
| ASD vs K | | -0.41 | N/A | -0.25 | N/A | -0.30 | N/A |
| ASA vs K | | 0.16 | | -0.21 | | -0.27 | |
| DS vs K | | -0.02 | | -0.18 | | -0.20 | |
| SF vs K | | 0.35 | | 0.10 | | 0.15 | |
| ZSD vs SF | | 0.23 | 0.13 | 0.04 | 0.13 | 0.09 | 0.23 |
| ZSA vs SF | | 0.16 | 0.1 | -0.06 | 0.12 | -0.03 | 0.35 |
| ZSD vs K | | 0.47 | N/A | 0.14 | N/A | -0.06 | N/A |
| ZSA vs K | | 0.52 | | 0.17 | | 0.05 | |
| ZSD vs DS | | 0.27 | 0.50 | -0.26 | 0.10 | -0.08 | 0.40 |
| ZSA vs DS | | 0.14 | 0.19 | -0.24 | 0.08 | -0.28 | 0.25 |
| ZSD vs ASD | | -0.32 | 0.36 | -0.06 | 0.10 | 0.32 | 0.32 |
| ZSA vs ASD | | -0.39 | 0.10 | -0.11 | 0.01 | 0.10 | 0.16 |
| ZSD vsASA | | 0.33 | 0.20 | 0.04 | 0.07 | 0.19 | 0.32 |
| ZSA vs ASA | | 0.37 | 0.02 | 0.02 | 0.17 | 0.03 | 0.22 |
| ZSD vs ZSA | | 0.92 | 0.52 | 0.89 | 0.40 | 0.67 | 0.43 |

The cluster power is equally distributed to the subpath power $P_{n,m}$, i.e., $P_{n,m} = \frac{P_n}{M}$.

**Path angles**: The departure and arrival azimuth angles are modeled as Gaussian distribution. We describe the procedure for the AoD only, since the same can be applied to the AoA. The model of the angle distribution is well matched only when the number of clusters is large enough that the angles can be randomly distributed. The azimuth AoD for the $n$-th cluster is generated by $\phi_{n,_{AoD}} = X_n\varphi_n + Y_n + \phi_{\text{LoS,AoD}}$ where $\phi_{\text{LoS,AoD}}$ is the LoS azimuth AoD and AoA at the TX and RX after their locations are defined in system simulations, and

$$\varphi_n = \frac{2\sigma_{\text{AS,D}}\sqrt{-\ln\left(P_n/\max\left(P_n\right)\right)}}{1.4C} \tag{7}$$

where $X_n \in \{1, -1\}$ is a uniformly distributed random variable, constant $C$ is a scaling factor related to the total number of clusters; $C$ is scaled to 0.9 in this model with fixed $N = 6$; $Y_n \sim \mathcal{N}\left(0, \sigma_{\text{AS,D}}/7\right)$ is another random variable. Finally, the subpath azimuth angles are calculated with a random intra-cluster offset angles $\alpha_m$, which is given by

$$\phi_{n,m,_{\text{AoD}}} = \phi_{n,_{\text{AoD}}} + \alpha_m \tag{8}$$

where $\alpha_m$ is a Laplacian random variable with zero mean and STD as the intra-cluster RMS azimuth spread of departure (ASD).

The ZoD and ZoA angles are generated as Laplacian random variables. The ZoD angle is generated similarly to AoD as $\theta_{n,_{ZoD}} = X_n\vartheta_n + Y_n + \theta_{\text{LoS,ZoD}} + \mu_{\text{Offset,ZoD}}$ where $\theta_{\text{LoS,AoD}}$ is the LoS ZoD direction at the TX and RX, and

$$\vartheta_n = \frac{\sigma_{\text{ZS,D}}\ln\left(P_n/\max(P_n)\right)}{C}. \tag{9}$$

where a scaling factor $C$ is set to 0.98. The ZSD $\sigma_{\text{ZS,D}}$ is an exponential random variable characterized by $\lambda_{\text{ZS,D}}$, which is a function of distance given by

$$1/\lambda_{\text{ZS,D}}(d_{\text{2D}}) = \max(\gamma_1 d_{\text{2D}} + \eta_1, \gamma_2 d_{\text{2D}} + \eta_2) \tag{10}$$

where $d_{\text{2D}}$ is the 2D distance between TX and RX and $\gamma, \eta$ is taken from Table V. The offset ZoD angle is modeled by

$$\mu_{\text{Offset,ZoD}}(d_{\text{2D}}) = -10^{(a_{\text{ZoD}}\log_{10}(\max(b_{\text{ZoD}}, d_{\text{2D}}))+c_{\text{ZoD}})}. \tag{11}$$

Then, the subpath ZoD angles are calculated with a random intra-cluster offset angles $\alpha_m$, which is given by

$$\theta_{n,m,_{ZoD}} = \theta_{n,_{ZoD}} + \alpha_m \tag{12}$$

where $\alpha_m$ is a Laplacian random variable with zero mean and STD referred to as intra-cluster ZSD. In the same manner, the ZoA angle is generated by following [33] and the ZSA is modeled as the dual-slope model given by

$$\mu_{\text{ZS,A}}(d_{\text{2D}}) = \max(\gamma_1 d_{\text{2D}} + \omega_1, \gamma_2 d_{\text{2D}} + \omega_2) \tag{13}$$

and the offset ZoA is modeled as a power function as,

$$\mu_{\text{Offset,ZoA}}(d_{\text{2D}}) = a_{\text{ZoA}}\left(d_{\text{2D}}\right)^{b_{\text{ZoA}}} + c_{\text{ZoA}}. \tag{14}$$

### B. Verification on Channel Model Output

The channel realization based on the stochastic channel model framework following 3D-SCM model, are compared to the measurement results and the ray-tracing results. Figure 11 shows the comparison of the reproduced RMS delay spread and ASD/ASA with measurements in the form of CDFs. Similar UMi statistics to those given here were found, using 28 GHz measurements and a 3GPP-like statistical simulator were derived from field measurements [18]. Delay spread and azimuth angular spread comparisons show that the values of the channel model outputs are comparable between measurement results and ray-tracing results. While more tuning could yield a better fit, the current channel models provide good agreement

Authorized licensed use limited to: K & L Gates. Downloaded on October 21,2025 at 14:40:17 UTC from IEEE Xplore. Restrictions apply.

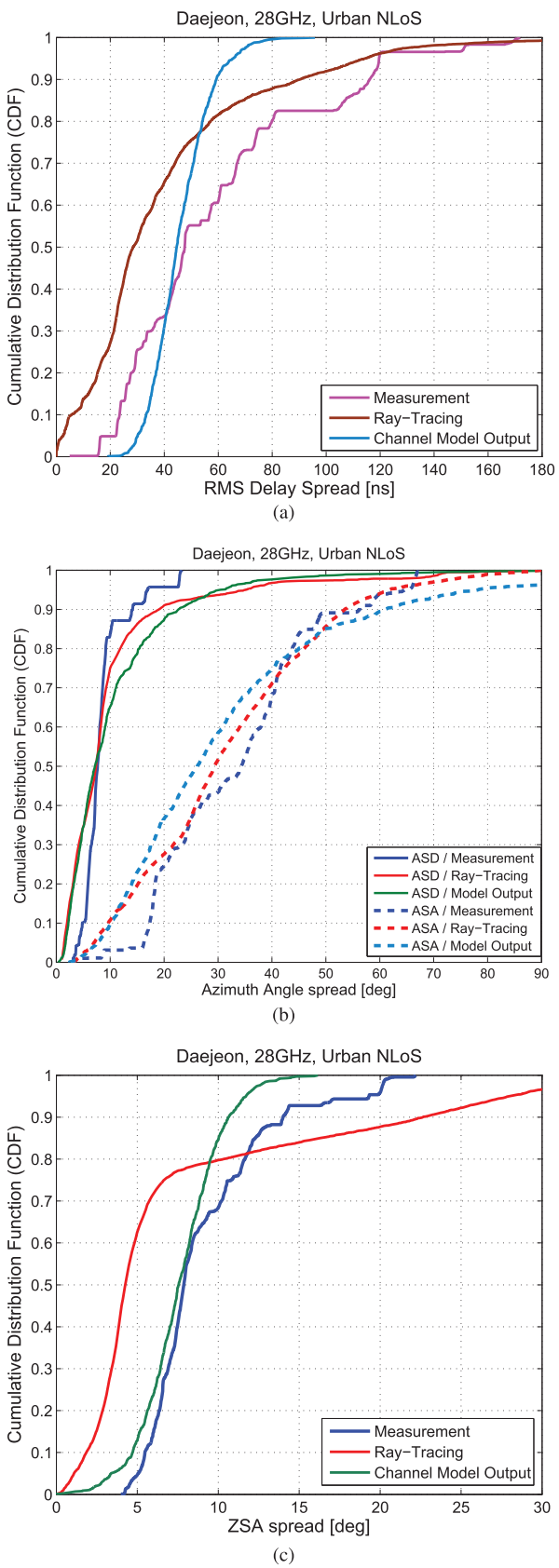


Fig. 11. Comparison of the measurement data and the ray-tracing simulation and the proposed channel model: (a) RMS Delay Spread, (b) AoD / AoA Azimuth Angle Spread and (c) ZoA Elevation Angle Spread in Daejeon.

for the measurements and ray-tracing. Generally, the stochastic channel model framework still works for the mmWave band.

In the path loss model in large-scale fading, the proposed path loss model based on ray-tracing uses up to 250 dB dynamic range, which is much higher than the limit of practical wideband channel sounders. As we discussed previously, given the pros and cons of applying the threshold of ray-tracing, the path loss models in the paper are not applied any threshold of path loss in order to emulate the model with higher sensitivity limit. It is observed and verified if the observation environments and the sensitivity levels are exactly same, the models derived both measurement and ray-tracing are similar, however, it is not shown yet the phenomenon far beyond any practical measured range. Thus, we are at the mercy of the ray tracer's accuracy in very weak signal conditions, without concrete assurances that the model is valid in these weak conditions. In previous sections, the ray-tracing has the limitation of the lack of details of geometry data base and lack of detailed scattering to emulate all physical phenomena. Also, the measurement conducted by the wideband channel sounder at mmWave frequency lacks link-budget to obtain enough dynamic range of the path loss model over 200 m range in NLoS environment. To the best of our understanding, we propose the path loss model as an extrapolation using the ray-tracing calibrated within the measurement distance range. For models at larger measurement or distance range, such as dual-slope models, it is required to validate the model with more measurement data to figure out what really happens beyond the current limit of channel sounder sensitivity level.

Note that the ray-tracing simulation was performed on grid samples with 1 m / 5 m spacing in this section, to average out the geometry-induced effects on channel modeling. It is also noted that the more ray-tracing samples provides slightly different characteristics in Section V compared to the simulation results used in the ray-tracing validations in Section III. In Section III, the 25 samples are located in the measurement points where the received power is not severely faded where the samples with dominant reflected paths have small angular spread, however, the samples in deep faded area have larger angular spread because there is no dominant path and similarly small received paths have larger angular spread.

## VI. Conclusion

In this paper, 3D-ray-tracing simulation is used to analyze the channel propagation characteristics at 28 GHz, where ray-tracing simulation is calibrated with measurement campaigns in the same area. Essential parameters for the 3GPP SCM framework were successfully obtained using the ray-tracing simulation that produces realistic multipath channels, for three urban scenarios covering UMi and UMa cases, where mmWave transmission for 5G mobile radio and other cellular communication system will be utilized in the future.

The proposed channel models in UMi and UMa urban scenarios are derived on LoS probability models, path loss models, and double-directional channel models. Using these models,

Authorized licensed use limited to: K & L Gates. Downloaded on October 21,2025 at 14:40:17 UTC from IEEE Xplore. Restrictions apply.

it is possible to extract several properties of mmWave radio channels. On path loss modeling, typical omni-directional path loss exponents are close to 3 in urban NLoS scenarios [18]. Moreover, the dual-slope path loss models are proposed which provide a more fitted path loss model from the propagation observations in street-canyon environments. We note that more measurements may be needed to validate the dual slope characteristic beyond 200 m and beyond 180 dB in measurement range. Averaged delay spread is observed to be less than 60 ns even in NLoS urban scenarios, and normalized average angular spread in mmWave band is observed to be within 40 degrees in the azimuth arrival direction. These observations are obtained from both measurements and ray-tracing results. The models of delay spread and angular spread in the channel follow a stochastic approach for a channel modeling framework provided with randomly modeled delay-angular spread parameters. These channel model parameters are provided, and the proposed channel model adapts the stochastic channel model framework usually utilized in performance evaluation methodology. The simulation results show that the stochastic channel model framework still works for mmWave channel.

In this paper, some features of mmWave channel model, such as blocking model including human blockage and dynamic shadow fading model, are not covered currently, and these features can be modeled as an additional module on the proposed channel model. These remain as future works.

## ACKNOWLEDGMENT

The authors would like to thank to Mathew K. Samimi of NYU for valuable discussions and Kuyeon Whang of Samsung for his work on enhancing the quality of the paper.

## REFERENCES

[1] S. Hur *et al.*, "28 GHz channel modeling using 3D ray-tracing in urban environments," in *Proc. Eur. Conf. Antennas Propag. (EuCAP)*, Apr. 2015, pp. 1–5.

[2] S. Baek, Y. Chang, S. Hur. J. Hwang, and B. Kim, "3-Dimensional large-scale channel model for urban environments in mmWave frequency," in *Proc. IEEE Int. Conf. Commun. Workshop (ICCW)*, Jun. 2015, pp. 1220–1225.

[3] W. Roh *et al.*, "Millimeter-wave beamforming as an enabling technology for 5 G cellular communications: Theoretical feasibility and prototype results," *IEEE Commun. Mag.*, vol. 52, no. 2, pp. 106–113, Feb. 2014.

[4] Z. Pi and F. Khan, "An introduction to millimeter-wave mobile broadband systems," *IEEE Commun. Mag.*, vol. 49, no. 6, pp. 101–107, Jun. 2011.

[5] T. S. Rappaport *et al.*, "Millimeter wave mobile communications for 5 G cellular: It will work!" *IEEE Access*, vol. 1, pp. 335–349, May 2013.

[6] Samsung Electronics. (2015). *5 G Vision White Paper* [Online]. Available: http://www.samsung.com/global/business-images/insights/2015/Samsung-5G-Vision-0.pdf

[7] J. Jarvelainen and K. Haneda, "Sixty gigahertz indoor radio wave propagation prediction based on full scattering model," in *Proc. Radio Sci.*, Apr. 2014, vol. 49, no. 4, pp. 293–305.

[8] G. Lovnes, J. Reis, and R. Raekken, "Channel sounding measurements at 59 GHz in city streets," in *Proc. IEEE Int. Symp. Pers. Indoor Mobile Radio Commun. (PIMRC'94)*, Sep. 1994, pp. 496–500.

[9] T. Manabe, Y. Miura, and T. Ihara, "Effects of antenna directivity and polarization on indoor multipath propagation characteristics at 60 GHz," *IEEE J. Sel. Areas Commun.*, vol. 14, no. 3, pp. 441–448, Apr. 1996.

[10] N. Daniele and C. Fort, "Outdoor millimetre-wave propagation measurements with line of sight obstructed by natural elements," *Electron. Lett.*, vol. 30, no. 18, pp. 1533–1534, Sep. 1994.

[11] H. Xu, T. S. Rappaport, R. J. Boyle, and J. H. Schaffner, "Measurements and models for 38-GHz point-to-multipoint radiowave propagation," *IEEE J. Sel. Areas Commun.*, vol. 18, no. 3, pp. 310–321, Mar. 2000.

[12] S. Y. Seidel and H. W. Arnold, "Propagation measurements at 28 GHz to investigate the performance of local multipoint distribution service (LMDS)," in *Proc. IEEE Global Telecommun. Conf. (GlobeCom)*, Nov. 1995, pp. 754–757.

[13] S. Wyne, K. Haneda, S. Ranvier, F. Tufvesson, and A. F. Molisch, "Beamforming effects on measured mm-Wave channel characteristics," *IEEE Trans. Wireless Commun.*, vol. 10, no. 1, pp. 3553–3559, Nov. 2011.

[14] C. Kim, J. Son, T. Kim, and J. Seol, "On the hybrid beamforming with shared array antenna for mmWave MIMO-OFDM systems," in *Proc. IEEE Wireless Commun. Netw. Conf. (WCNC)*, Apr. 2014, pp. 335–340.

[15] S. Sun *et al.*, "MIMO for millimeter-wave wireless communications: Beamforming, spatial multiplexing, or both?" *IEEE Commun. Mag.*, vol. 52, no. 12, pp. 110–121, Dec. 2014.

[16] METIS. (2015). *Mobile and Wireless Communications Enablers for the Twenty-Twenty Information Society, D1.4, METIS Channel Models*, [Online]. Available: http://www.metis2020.com

[17] MiWEBA. (2014). *Millimetre-Wave Evolution for Backhaul and Access, D5.1, Channel Modeling and Characterization* [Online]. Available: http://www.miweba.eu

[18] T. S. Rappaport, G. Maccartney, M. K. Samimi, and S. Sun, "Wideband millimeter-wave propagation measurements and channel models for future wireless communication system design," *IEEE Trans. Commun.*, vol. 63, no. 9, pp. 3029–3056, Sep. 2015.

[19] G. MacCartney, T. S. Rappaport, S. Sun, and S. Deng, "Indoor office wideband millimeter-wave propagation measurements and channel models at 28 GHz and 73 GHz for ultra-dense 5 G wireless networks," *IEEE Access*, vol. 3, pp. 2388–2424, Oct. 2015.

[20] M. Samimi *et al.*, "Statistical channel model with multi-frequency and arbitrary antenna beamwidth for millimeter-wave outdoor communications," in *Proc. IEEE Global Commun. Conf. (GLOBECOM) Workshop*, Dec. 2015, pp. 1–7.

[21] S. Sun *et al.*, "Synthesizing omnidirectional antenna patterns, received power and path loss from directional antennas for 5 G millimeter-wave communications," in *Proc. IEEE Global Commun. Conf. (GLOBECOM)*, Dec. 2015, pp. 1–7.

[22] M. K. Samimi and T. S. Rappaport, "Local multipath model parameters for generating 5 G millimeter-wave 3GPP-like channel impulse response," in *Proc. Eur. Conf. Antennas Propag. (EuCAP)*, Apr. 2016, pp. 1–5.

[23] mmMagic. (2016). *mm-Wave Based Mobile Radio Access Network for 5G Integrated Communications, W2.1, 6-100 GHz Channel Modelling for 5G: Measurement and Modelling Plans in mmMAGIC*, [Online]. Available: https://5g-mmmagic.eu

[24] S. Hur *et al.*, "Wideband spatial channel model in an urban cellular environments at 28 GHz," in *Proc. Eur. Conf. Antennas Propag. (EuCAP)*, Apr. 2015, pp. 1–5.

[25] M. K. Samimi and T. S. Rappaport, "3-D statistical channel models for millimeter-wave outdoor mobile broadband communications," in *Proc. IEEE Int. Conf. Commun. (ICC)*, Jun. 2015, pp. 2430–2436.

[26] S. Nie, G. R. MacCartney, S. Sun, and T. S. Rappaport, "28 GHz and 73 GHz signal outage study for millimeter wave cellular and backhaul communications," in *Proc. IEEE Int. Conf. Commun. (ICC)*, Jun. 2014, pp. 4856–4861.

[27] S. Y. Seidel and T. S. Rappaport, "Site-specific propagation prediction for wireless in-building personal communication system design," *IEEE Trans. Veh. Technol.*, vol. 43, no. 4, pp. 879–891, Nov. 1994.

[28] C. Oestges, "Experimental validation of ray-tracing at 12 and 30 GHz," COST IC1004 TD(14)11002, Sep. 2014.

[29] H. C. Nguyen *et al.*, "Evaluation of empirical ray-tracing model for urban outdoor scenario at 73 GHz," in *Proc. IEEE Veh. Technol. Conf. (VTC-Fall)*, Sep. 2014, pp. 1–6.

[30] K. R. Schaubach, N. J. Davis IV, and T. S. Rappaport, "A ray tracing method for predicting path loss and delay spread in microcellular environments," in *Proc. IEEE Veh. Technol. Conf. (VTC'92)*, May 1992, pp. 932–935.

[31] T. S. Rappaport, R. W. Heath Jr., R. Daniels, and J. Murdock, *Millimeter Wave Wireless Communications*. Englewood Cliffs, NJ, USA: Pearson/Prentice-Hall, 2015.

[32] K. Haneda, "Channel models and beamforming at millimeter-wave frequency bands," *IEICE Trans. Commun.*, vol. E98, no. 5, pp. 755–772, May 2015.

[33] 3GPP TR 36.873, "Study on 3D channel model for LTE," Sep. 2014.

Authorized licensed use limited to: K & L Gates. Downloaded on October 21,2025 at 14:40:17 UTC from IEEE Xplore. Restrictions apply.

[34] IST-4-027756 WINNER II, "D1.1.2, WINNER II channel models," Sep. 2007.
[35] Report ITU-R M.2135, "Guidelines for evaluation of radio interface technologies for IMT-advanced," 2008.
[36] S. Hur, Y.-J. Cho, J. Lee, N.-G. Kang, J. Park, and H. Benn, "Synchronous channel sounder using horn antenna and indoor measurements on 28 GHz," in *Proc. IEEE Int. Black Sea Conf. Commun. Netw. (BlackSeaCom)*, May 2014, pp. 83–87.
[37] G. R. MacCartney Jr., M. K. Samimi, and T. S. Rappaport, "Omnidirectional path loss models at 28 GHz and 73 GHz in New York City," in *Proc. IEEE Int. Symp. Pers. Indoor Mobile Radio Commun.*, Sep. 2014, pp. 227–231.
[38] M. Marcus and B. Pattan, "Millimeter wave propagation: Spectrum management implications," *IEEE Microw. Mag.*, vol. 6, no. 2, pp. 54–62, Jun. 2005.
[39] Remcom, *Wireless InSite Reference Manual*, ver. 2.7.1, Commercial SW user-manual, Mar. 2014.
[40] ITU-R P.2040, "Effects of building materials and structures on radiowave propagation above about 100 MHz," International Telecommunication Union Radiocommunication Sector ITU-R, 2013.
[41] L. M. Correia and P. O. Frances, "Estimation of materials characteristics from power measurements at 60 GHz," in *Proc. IEEE Int. Symp. Pers. Indoor Mobile Radio Commun. (PIMRC)*, Sep. 1994, pp. 510–513.
[42] M. Lott and I. Forkel, "A multi-wall-and-floor model for indoor radio propagation," in *Proc. IEEE Veh. Technol. Conf. (VTC)*, 2001, pp. 464–468.
[43] V. Degli-Esposti *et al.*, "Polarimetric analysis of mm-Wave propagation for advanced beamforming applications," in *Proc. Eur. Conf. Antennas Propag. (EuCAP'15)*, Apr. 2015, pp. 1–4.
[44] K. Belbase, M. Kim, and J. Takada, "Study of propagation mechanisms and identification of scattering objects in indoor multipath channels at 11 GHz," in *Proc. Eur. Conf. Antennas Propag. (EuCAP)*, Apr. 2015, pp. 1–4.
[45] M. Steinbauer, "The radio propagation channel: a non-directional, directional, and double-directional point-of-view," Ph.D. dissertation, Vienna Univ. Tech., Inst. Commun. RadioFreq. Eng., Vienna, Austria, 2001.
[46] M. K. Samimi, T. S. Rappaport, and G. R. MacCartney, Jr., "Probabilistic omnidirectional path loss models for millimeter-wave outdoor communications," *IEEE Wireless Commun. Lett.*, vol. 4, no. 4, pp. 357–360, Mar. 2015.
[47] T. S. Rappaport, *Wireless Communications: Principles and Practice*, 2nd ed. Englewood Cliffs, NJ, USA: Prentice-Hall, 2002.
[48] Y. Chang, S. Baek, S. Hur, Y. Mok, and Y. Lee, "A novel dual-slope mm-Wave channel model based on 3D ray-tracing in urban environments," in *Proc. IEEE Int. Symp. Pers. Indoor Mobile Radio Commun. (PIMRC)*, Sep. 2014, pp. 222–226.
[49] S. Sun, T. A. Thomas, T. S. Rappaport, H. Nguyen, I. Z. Kovacs, and I. Rodriguez, "Path loss, shadow fading, and line-of-sight probability models for 5 G urban macro-cellular scenarios," in *Proc. IEEE Global Commun. Conf. Workshop (Globecom Workshop)*, Dec. 2015, pp. 1–7.
[50] C. Gustafson, T. Abbas, D. Bolin, and F. Tufvesson, "Statistical modeling and estimation of censored pathloss data," *IEEE Wireless Commun. Lett.*, vol. 4, no. 5, pp. 1–7, Oct. 2015.
[51] H. C. Nguyen, I. Rodriguez, T. Sørensen, L. Sanchez, I. Kovacs, and P. Mogensen, "An empirical study of urban macro propagation at 10, 18 and 28 GHz," in *Proc. IEEE Veh. Technol. Conf. (VTC'16-Spring)*, Feb. 2016, pp. 1–5.
[52] C. Gustafson, T. Abbas, D. Bolin, and F. Tufvesson, "Statistical modeling and estimation of censored pathloss data," *IEEE Wireless Commun. Lett.*, vol. 4, no. 5, pp. 1–5, Oct. 2015.
[53] N. Czink, "The random-cluster model a stochastic MIMO channel model for broadband wireless communication systems of the 3rd generation and beyond," Ph.D. dissertation, Vienna Univ. Tech., Inst. Commun. RadioFreq. Eng., Vienna, Austria, 2007 [Online]. Available: http://publik.tuwien.ac.at/files/PubDat112121.pdf
[54] D.-J. Kim, Y. W. Park, and D.-J. Park, "A novel validity index for determination of the optimal number of clusters," *IEICE Trans. Inf. Syst.*, vol. 38, no. 2, pp. 281–285, Feb. 2001.
[55] C. Gustafson, K. Haneda, S. Wyne, and F. Tufvesson, "On mm-Wave multipath clustering and channel modeling," *IEEE Trans. Antennas Propag.*, vol. 62, no. 3, pp. 1445–1455, Mar. 2014.
[56] G. Calcev *et al.*, "A wideband spatial channel model for system-wide simulations," *IEEE Trans. Veh. Techol.*, vol. 56, no. 2, pp. 389–403, Mar. 2007.

**Sooyoung Hur** (S'05–M'13) received the B.S. degree from Sogang University, Seoul, Korea, in 2005, and the M.S. degree from Korea Advanced Institute of Science and Technology (KAIST), Daejeon, Korea, in 2007, both in electrical engineering, and the Ph.D. degree in electrical and computer engineering from Purdue University, West Lafayette, IN, USA, in 2013. Since 2013, he has been with Samsung Electronics in the Communication Research Team. His research interests include physical layer communications and in particular channel measurements, cellular and mmWave communications, and signal processing for wireless communications, especially 5G communication technologies.

**Sangkyu Baek** (M'12) received the B.S. degrees in both mathematics and telecommunications mathematics, and the M.S. and Ph.D. degrees in mathematics from Korea University, Seoul, Korea, in 2006, 2008, and 2011, respectively. From 2011 to 2012, he was a Postdoctoral Researcher with the Department of Electrical Engineering, Korea University. Since 2012, he has been with Communication Research Team, Samsung Electronics, Suwon, Korea. He is currently working on design and development of medium access control protocol and channel model for 5G communications. His research interests include probability theory, queueing theory, and analytical performance evaluation of wireless communications systems.

**Byungchul Kim** (M'09) received the Ph.D. degree in electronic and computer engineering from Pohang University of Science and Technology (POSTECH), Pohang, Korea, in 2009. Since he joined Samsung Electronics in 2009, he has mainly been engaged in research and development of antennas. His research interests include mmWave antenna design and propagation analysis for 5G wireless communication technologies.

**Youngbin Chang** (M'02) is currently pursuing the Ph.D. degree in electronic engineering at Korea University, Seoul, Korea. He joined Samsung Electronics in 2002, he is now working for Communication Research Team, as a Principle Engineer. He has mainly designed wireless communication systems. He has also actively participated in international standards such as the IEEE 802.16 and 3GPP LTE. His research interests include LTE evolution and next generation communication technologies, especially device to device communications, mmWave channel modeling, mobility control and 5G radio protocol design.

Authorized licensed use limited to: K & L Gates. Downloaded on October 21,2025 at 14:40:17 UTC from IEEE Xplore. Restrictions apply.

**Andreas F. Molisch** (S'89–M'95–SM'00–F'05) received the Dipl. Ing., Ph.D., and Habilitation degrees from the Technical University of Vienna, Vienna, Austria, in 1990, 1994, and 1999, respectively. He subsequently was with AT&T (Bell) Laboratories Research (USA); Lund University, Lund, Sweden, and Mitsubishi Electric Research Labs, Cambridge, MA, USA. He is now a Professor of Electrical Engineering and the Director of the Communication Sciences Institute with the University of Southern California, Los Angeles, CA, USA. His research interests include the measurement and modeling of mobile radio channels, ultra-wideband communications and localization, cooperative communications, multiple-input–output systems, wireless systems for healthcare, and novel cellular architectures. He has authored, coauthored, or edited four books [among them the textbook *Wireless Communications* (Wiley-IEEE Press)], 16 book chapters, some 180 journal papers, 260 conference papers, as well as more than 80 patents and 70 standards contributions. He has been an Editor of a number of journals and special issues, the General Chair, Technical Program Committee Chair, or Symposium Chair of multiple international conferences, as well as the Chairman of various international standardization groups. He is a Fellow of the National Academy of Inventors, the AAAS, the IET, an IEEE Distinguished Lecturer, and a member of the Austrian Academy of Sciences. He was the recipient of numerous awards, among them the Donald Fink Prize of the IEEE, and the Eric Sumner Award of the IEEE.

**Theodore (Ted) S. Rappaport** (S'83–M'84–SM'91–F'98) is the David Lee/Ernst Weber Professor of Electrical and Computer Engineering with the New York University (NYU) Tandon School of Engineering, Brooklyn, NY, USA, and the Founding Director of the NYU WIRELESS Research Center. He also holds professorship positions with the Courant Institute of Mathematical Sciences and the NYU School of Medicine. He founded major wireless research centers at the Virginia Polytechnic Institute, Blacksburg, VA, USA, and State University (MPRG), The University of Texas at Austin, Austin, TX, USA (WNCG), and New York University, New York, NY, USA (NYU WIRELESS), and founded two wireless technology companies (TSR Technologies, Inc. and Wireless Valley Communications, Inc.) that were sold to publicly traded firms. He is a highly sought-after technical consultant and corporate advisor, having testified before the U.S. Congress and having served the ITU. He has advised more than 100 students, holds more than 100 patents issued and pending, and has authored or coauthored several books, including the best-seller *Wireless Communications: Principles and Practice* (Second Edition, Prentice Hall, 2002). His latest book, entitled *Millimeter Wave Wireless Communications* (Pearson/Prentice Hall, 2015), is the first comprehensive text on the subject. He has served on the board of governors of the IEEE COMMUNICATIONS AND VEHICULAR TECHNOLOGY societies. He is an avid amateur radio operator, with the call sign N9NB, and is a life member of the American Radio Relay League, and also enjoys long distance running. He was the recipient of the numerous recognitions for his work as a researcher and educator, including the IEEE Donald Fink Prize Paper Award, the ASEE Terman Award, the IET Sir Monty Finniston Award, the IEEE Communications Society Edwin H. Armstrong Award, the William Sayle education award from the IEEE Education Society, the Stuart F. Meyer Award from the IEEE Vehicular Technology Society, the Sarnoff citation from the Radio Club of America, and the Marconi Young Scientist Award.

**Katsuyuki Haneda** (S'03–M'07) received the doctor of engineering degree from Tokyo Institute of Technology, Tokyo, Japan, in 2007. He is presently an Assistant Professor with the School of Electrical Engineering, Aalto University, Espoo, Finland. His research interests include high-frequency radios such as millimeter-wave and beyond, wireless for medical and postdisaster scenarios, radio wave propagation modeling, and in-band full-duplex radio technologies. He has been serving as an Associate Editor for the IEEE TRANSACTIONS ON ANTENNAS AND PROPAGATION, since 2012, and as an Editor of the IEEE TRANSACTIONS ON WIRELESS COMMUNICATIONS since 2013. He has also been an active member of a number of European COST Actions, e.g., IC1004 Cooperative radio communications for green smart environments and CA15104 Inclusive Radio Communication Networks for 5G and beyond (IRACON). He was the recipient of the Best Paper Award of the antennas and propagation track in the IEEE 77th Vehicular Technology Conference (VTC2013-Spring), Dresden, Germany, and of the Best Propagation Paper Award in the 7th European Conference on Antennas and Propagation (EuCAP2013), Gothenburg, Sweden.

**Jeongho Park** (M'05) received the Ph.D. degree in electronic engineering from Yonsei University, Seoul, Korea. Since he joined Samsung Electronics in 2005, he has mainly been engaged in research and development of wireless communications. Standardization is also his interest including the IEEE 802, the 3GPP RAN, and the ITU-R IMT-Systems. Currently, he is the Director of Communications Research Team at Samsung Electronics Mobile Communications Business. His research interests include 5G technologies and cellular internet of things (IoT).

Authorized licensed use limited to: K & L Gates. Downloaded on October 21,2025 at 14:40:17 UTC from IEEE Xplore. Restrictions apply.